
SKI to go Faster: Accelerating Toeplitz Neural Networks via Asymmetric Kernels

Alexander Moreno*
Luminous Computing
alexander.f.moreno@gmail.com

Jonathan Mei*
Luminous Computing
j@mei.to

Luke Walters*
Luminous Computing
lukecwalters@gmail.com

Abstract

Toeplitz Neural Networks (TNNs) [1] are a recent sequence model with impressive results. They require $O(n \log n)$ computational complexity and $O(n)$ relative positional encoder (RPE) multi-layer perceptron (MLP) and decay bias calls. We aim to reduce both. We first note that the RPE is a non-SPD (symmetric positive definite) kernel and the Toeplitz matrices are pseudo-Gram matrices. Further 1) the learned kernels display spiky behavior near the main diagonals with otherwise smooth behavior; 2) the RPE MLP is slow. For bidirectional models, this motivates a sparse plus low-rank Toeplitz matrix decomposition. For the sparse component’s action, we do a small 1D convolution. For the low rank component, we replace the RPE MLP with linear interpolation and use asymmetric Structured Kernel Interpolation (SKI) [2] for $O(n)$ complexity: we provide rigorous error analysis. For causal models, “fast” causal masking [3] negates SKI’s benefits. Working in the frequency domain, we avoid an explicit decay bias. To enforce causality, we represent the kernel via the real part of its frequency response using the RPE and compute the imaginary part via a Hilbert transform. This maintains $O(n \log n)$ complexity but achieves an absolute speedup. Modeling the frequency response directly is also competitive for bidirectional training, using one fewer FFT. We set a speed state of the art on Long Range Arena [4] with minimal score degradation.

1 Introduction

Sequence modeling is important in natural language processing, where sentences are represented as a sequence of tokens, and a token’s representation can both influence and be influenced by the context of surrounding tokens. Successful sequence modeling typically involves token and channel mixing. Token mixing combines representations of different parts of the sequence, while channel mixing combines the information across different dimensions of embedding vectors used to encode tokens and their intermediate representations within a neural network. Transformers [5] and more generally xFormers are arguably the most successful technique for sequence modeling, and variants including [6, 7] have achieved state of the art performance on natural language tasks. They use self-attention for token mixing and feedforward networks for channel mixing.

*All authors contributed equally. Alexander and Jonathan flipped for ordering.

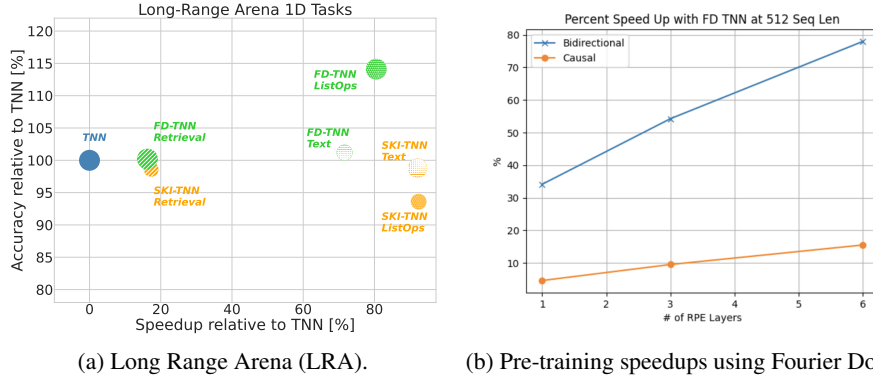


Figure 1: (a) In LRA, our approach, SKI-TNN is faster than all previous approaches with strong LRA score. Bubble sizes denote training model memory. (b) Our approach, FD-TNN, achieves substantial speed ups in iterations/sec for pre-training both causal and bidirectional models. Note that we do not include SKI-TNN in this plot as it does not use an MLP based RPE.

Recently, [1] proposed Toeplitz Neural Networks (TNN) using Toeplitz matrices for token mixing, applying a different linear system per channel. They use a learned neural similarity function, the Relative Positional Encoder (RPE), to form the Toeplitz matrices. Toeplitz matrix vector multiplication can be performed with sub-quadratic complexity using the Fast Fourier Transform (FFT), giving the TNN token mixing layer a total $O(dn \log n)$ computational complexity, where d is the embedding dimension and n is the sequence length. This achieved state of the art predictive performance and nearly state of the art speed for the long range arena (LRA) benchmark [4]. They also showed strong performance pre-training wikitext-103 [8] and on the GLUE benchmark[9]. Despite their strong empirical speed performance, TNNs have two fundamental efficiency limitations: 1) super-linear computational complexity 2) many calls to the RPE: for each layer, one call per relative position.

In this paper, we interpret the RPE as a non-SPD kernel, and note 1) the learned kernels are discontinuous near the main diagonals but otherwise smooth globally; 2) the ReLU RPE learns a 1D piecewise linear function: an MLP is slower than necessary. For bidirectional models, this motivates a sparse plus low-rank decomposition. We apply the sparse component’s action via a small 1D convolution. For the low rank component, we replace the RPE MLP with linear interpolation at a set of inducing points and an asymmetric extension of Structured Kernel Interpolation (SKI) [2] for $O(n)$ complexity. Further, using an inverse time warp, we can extrapolate beyond sequence lengths observed during training. For causal models, even “fast” causal masking [3] negates the speed and memory benefits from SKI. Thus, we instead represent the real part of the kernel’s frequency response using the RPE MLP, and evaluate the RPE with finer frequency resolution to extrapolate to longer sequence lengths in the time domain. From the real part, we compute the imaginary part via a Hilbert transform during the forward pass to enforce causality. In the bidirectional setting, we remove the causality constraint and represent the complex frequency response of the kernel with the RPE MLP. Levels of smoothness in frequency response imply decay rates in the time domain: thus we model the decay bias implicitly. This maintains $O(n \log n)$ complexity but achieves an absolute speedup.

This paper has three primary contributions: 1) a TNN sparse plus low rank decomposition, extending SKI to TNNs for the low rank part. We replace the RPE MLP with linear interpolation and apply inverse time warping to efficiently train bidirectional language models. We provide rigorous error analysis for our asymmetric SKI application; 2) alternatively, for both causal and bidirectional models, we work directly in the frequency domain and use the Hilbert transform to enforce causality in the autoregressive setting. We prove that different activation choices for an MLP modeling the discrete time Fourier transform (DTFT) lead to different decay rates in the original kernel. 3) Empirical results: we demonstrate that our approaches show dramatically improved computational efficiency, setting a new speed state of the art on LRA [10], with minimal deterioration of predictive performance. In section 2 we describe related work. In section 3 we propose our new modeling approaches. In 4 we state several theoretical results regarding our modeling approaches. In 5 we extend the empirical results of [1], showing our speed gains with minimal prediction deterioration. We conclude in section 6 with a discussion of limitations and future work.

2 Related

The most related papers use Toeplitz matrices for sequence modeling [1, 11, 12]. We build off of [1] and introduce several techniques to improve on their speed results. [11] took a similar approach, but applied Toeplitz matrices to self-attention rather than departing from it. [12] is also similar, using alternating Toeplitz and diagonal matrices as a replacement for self-attention within a Transformer. While we focus on the setting of [1] as it was released first, our approach is applicable to [12].

Also related are kernel based xFormers, particularly those using the Nyström method [13, 14]. The most related work is Nyströmformer [15], which adapts a matrix Nyström method for asymmetric matrices [16] to self-attention. We instead adapt this along with SKI [2] to Toeplitz matrices. Skyformer [17] extends Nyströmformer by embedding the self-attention matrix into a larger PSD kernel matrix and approximating the larger matrix instead. They show that their final approximate matrix has lower spectral error compared to Nyströmformer and leads to higher average validation accuracy on LRA [4]. The tradeoff, however, is that their method is slightly slower than Nyströmformer. Also somewhat related are the random feature approximations to self-attention [18, 19]. These extend [20], but use different random features that better approximate self-attention than random Fourier or binning features. For instance, [19] proposed positive random features.

Sparse transformer papers are also relevant. [21] proposed using both strided and fixed patterns. [22] alternated between sparse locally banded and dense attention. Finally, [23] proposed combining random attention, window attention and global attention. Our use of a short convolutional filter is most similar to window attention. Note that the space of efficient transformers is huge and there are many models that we haven't covered that may be relevant. [10] provides an excellent survey.

Other recent successful long sequence approaches include state space based approaches [24, 25, 26], long convolution based approaches [27, 28], adding moving averages to gated attention [29] and other alternatives to Transformer blocks [30].

3 Modeling Approach

We first review Toeplitz matrices and Toeplitz neural networks (TNNs) in section 3.1. We then analyze how to make the Toeplitz neural operator (TNO), the main computational bottleneck of the TNN, faster. We discuss our Nyström and SKI based approaches to speed up bidirectional training in 3.2. We then discuss our approach to causal training using the Hilbert transform in 3.3.

3.1 Preliminaries: Toeplitz matrices and Toeplitz Neural Networks

TNNs [1] replace self-attention, which computes the action of self-attention matrices that encode the similarity between both observation values and absolute positions, with the action of Toeplitz matrices that encode similarity only based on *relative* positions. Toeplitz matrices have, for each diagonal, the same entries from left to right. That is,

$$\mathbf{T}_{ij} = t_{i-j}, \mathbf{T} \in \mathbb{R}^{n \times n}$$

Unlike self-attention matrices, which require $O(n^2)$ memory, a Toeplitz matrix has $2n - 1$ unique elements and requires $O(n)$ memory. Due to close connections with discrete-time convolution, $\mathbf{T}\mathbf{x}$ can be computed in $O(n \log n)$ time by embedding \mathbf{T} in a circulant matrix and applying FFT.

A TNN [1] has multiple sequence modeling blocks, which we show in Figure 3 in Appendix A. Each block has a Gated Toeplitz Unit (GTU), which does both token and channel mixing, followed by a Gated Linear Unit (GLU) [31], which does channel mixing. The core of the GTU is the Toeplitz Neural Operator (TNO), which does token mixing and is the part of the architecture that we modify.

We now describe the TNO, shown in Figure 3b of Appendix A. Given a sequence $\mathbf{X} \in \mathbb{R}^{n \times d}$ of length n and dimension d in discrete time, there are $2n - 1$ unique relative positions/times $i - j$ for $i, j = 1, \dots, n$. Each relative position gets mapped to an embedding via an RPE $: \mathbb{Z} \rightarrow \mathbb{R}^d$, a neural network that maps a relative position to a d -dimensional embedding. These embeddings are used to construct Toeplitz matrices \mathbf{T}^l for $l = 1, \dots, d$ using

$$\mathbf{T}_{ij}^l = \lambda^{|i-j|} \text{RPE}_l(i - j).$$

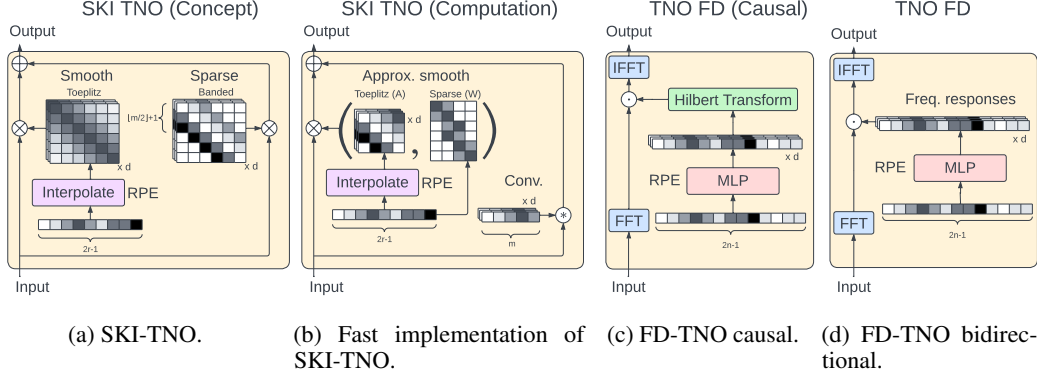


Figure 2: Our SKI-TNO and FD-TNO modifications: (a) We decompose Toeplitz matrices into sums of sparse + smooth components. Additionally, we use interpolation instead of an MLP to learn the RPE. (b) We use a 1D convolution to apply the sparse component and SKI as a low-rank approximation to the smooth component. (c) For the causal case, we use frequency domain RPE with a Hilbert Transform to enforce causality. (d) Our FD-TNO also is competitive in the bidirectional case, with one fewer FFT than TNO.

$\text{RPE}_l(i - j)$ is a learned similarity between positions for dimension l , while $\lambda^{|i-j|}$ with $\lambda \in (0, 1)$ is an exponential decay bias penalizing far away tokens to be dissimilar. Intuitively, we can interpret \mathbf{T}_{ij}^l as evaluating a stationary non-SPD kernel $k_l(i - j) = \lambda^{|i-j|} \text{RPE}_l(i - j)$. Thus \mathbf{T}^l can be interpreted as a pseudo or generalized Gram matrix. Letting \mathbf{x}^l be the l th column of \mathbf{X} , the TNO outputs

$$\text{TNO}(\mathbf{X}) = (\mathbf{T}^1 \mathbf{x}^1 \dots \mathbf{T}^d \mathbf{x}^d) \in \mathbb{R}^{n \times d}$$

where each $\mathbf{T}^l \mathbf{x}^l$ is computed via the FFT as described above.

The main costs are the RPE’s MLP, the FFT, and the decay bias $\lambda^{|i-j|}$. We aim to eliminate the MLP and the decay bias when possible. In the bidirectional setting, we apply the FFT using a much smaller Toeplitz matrix. In the causal setting, we learn the RPE’s frequency response directly.

3.2 Bidirectional Training

For a given Toeplitz matrix \mathbf{T} , we assume it admits a decomposition that we can approximate with a sparse+low-rank representation, $\mathbf{T} = \mathbf{T}_{\text{sparse}} + \mathbf{T}_{\text{smooth}} \approx \mathbf{T}_{\text{sparse}} + \mathbf{T}_{\text{low}}$. Our bidirectional training thus consists of three primary components. The first, the sparse component $\mathbf{T}_{\text{sparse}}$ is straightforward. Applying the action $\mathbf{T}_{\text{sparse}} \mathbf{x}$ of $\mathbf{T}_{\text{sparse}} \in \mathbb{R}^{n \times n}$ with m non-zero diagonals is equivalent to applying a 1D convolution layer with filter size m . We then discuss our asymmetric SKI for \mathbf{T}_{low} in section 3.2.1. Finally, we discuss how we handle sequence lengths not observed in training for \mathbf{T}_{low} via an inverse time warp in section 3.2.2. Algorithm 1 summarizes our TNO based on these techniques.

Algorithm 1 Sparse Plus Low Rank Bidirectional TNO with Asymmetric SKI

Given sequence $\mathbf{X} \in \mathbb{R}^{n \times d}$ with columns \mathbf{x}^l
Hyperparameters rank $r \ll n$, sparse filter size m , interpolation degree N , decay parameter λ
Compute inducing points p_1, \dots, p_r evenly spaced on $[0, n]$
for $l = 1, \dots, d$ **do**
 Compute $\mathbf{T}_{\text{sparse}}^l \mathbf{x}^l$ with a 1D convolutional filter, size m .
 Let $x(t) = \text{sign}(t) \lambda^{|t|}$.
 Form $\mathbf{A}^l \in \mathbb{R}^{r \times r}$ with entries $\mathbf{A}_{ij}^l = k_l(p_i - p_j) = \text{RPE}_l(x(p_i - p_j))$
 Form $\mathbf{W}^l \in \mathbb{R}^{n \times r}$ degree N polynomial interpolation matrix
 Compute $\mathbf{T}_{\text{low}}^l \mathbf{x}^l$ with $\mathbf{T}_{\text{low}}^l = \mathbf{W}^l \mathbf{A}^l \mathbf{W}^{l\top}$
end for
Return $\text{TNO}(\mathbf{X}) = (\mathbf{T}_{\text{sparse}}^1 \mathbf{x}^1 + \mathbf{T}_{\text{low}}^1 \mathbf{x}^1, \dots, \mathbf{T}_{\text{sparse}}^d \mathbf{x}^d + \mathbf{T}_{\text{low}}^d \mathbf{x}^d)$

3.2.1 SKI For Asymmetric Nyström

Given an asymmetric stationary kernel k , we wish to approximate the (pseudo) Gram matrix $\mathbf{T} \in \mathbb{R}^{n \times n}$ using a low-rank approximation based on a smaller Gram matrix $\mathbf{A} \in \mathbb{R}^{r \times r}$, with $r \ll n$. In context, \mathbf{A} is formed using relative positions between a set of inducing points p_1, \dots, p_r instead of the full set $1, \dots, n$ that is used for \mathbf{T} . That is,

$$\mathbf{T}_{ij} = k(i - j) \quad \text{and} \quad \mathbf{A}_{ij} = k(p_i - p_j).$$

In our case, the inducing points are uniformly spaced. Some submatrices of \mathbf{A} may be submatrices of \mathbf{T} (i.e. if inducing points are also observation points). To derive the Nyström approximation, we form an augmented Gram matrix $\mathbf{K} \in \mathbb{R}^{(n+r) \times (n+r)}$ in block form as

$$\mathbf{K} = \begin{pmatrix} \mathbf{A} & \mathbf{B} \\ \mathbf{F} & \mathbf{T} \end{pmatrix},$$

where $\mathbf{B} \in \mathbb{R}^{r \times n}$ and $\mathbf{F} \in \mathbb{R}^{n \times r}$ are respectively the upper right and lower left partitions of the large Gram matrix \mathbf{K} . Explicitly,

$$\mathbf{B}_{ij} = k(p_i - j) \quad \text{and} \quad \mathbf{F}_{ij} = k(i - p_j).$$

Extending [16] to allow singular \mathbf{A} ,

$$\hat{\mathbf{K}} = \begin{pmatrix} \mathbf{A} \\ \mathbf{F} \end{pmatrix} \mathbf{A}^\dagger (\mathbf{A} \quad \mathbf{B}) = \begin{pmatrix} \mathbf{A} & \mathbf{A}\mathbf{A}^\dagger\mathbf{B} \\ \mathbf{F}\mathbf{A}^\dagger\mathbf{A} & \mathbf{F}\mathbf{A}^\dagger\mathbf{B} \end{pmatrix}$$

where \mathbf{A}^\dagger is the Moore-Penrose pseudo-inverse satisfying $\mathbf{A}\mathbf{A}^\dagger\mathbf{A} = \mathbf{A}$ (but not necessarily $\mathbf{A}\mathbf{A}^\dagger = \mathbf{I}$ as in [16], which shows up in our different expressions for off-diagonal blocks of $\hat{\mathbf{K}}$). Following structured kernel interpolation (SKI) [2], we approximate \mathbf{F} and \mathbf{B} using interpolation. Specifically,

$$\mathbf{F} \approx \mathbf{W}\mathbf{A} \quad \text{and} \quad \mathbf{B} \approx \mathbf{A}\mathbf{W}^\top$$

where $\mathbf{W} \in \mathbb{R}^{n \times r}$ is a matrix of sparse interpolation weights with up to two non-zero entries per row for linear interpolation or up to four for cubic. These weights can be computed in closed form from the inducing points p_i and the observation points i . Thus we have

$$\begin{aligned} \mathbf{T} &\approx \mathbf{F}\mathbf{A}^\dagger\mathbf{B} \approx \mathbf{W}\mathbf{A}\mathbf{A}^\dagger\mathbf{A}\mathbf{W}^\top = \mathbf{W}\mathbf{A}\mathbf{W}^\top \\ &\Rightarrow \tilde{\mathbf{T}} = \mathbf{W}\mathbf{A}\mathbf{W}^\top \end{aligned}$$

as desired. We can set $\mathbf{T}_{\text{low}} = \tilde{\mathbf{T}}$ and compute $\tilde{\mathbf{T}}\mathbf{x}$ by first applying $\mathbf{W}^\top\mathbf{x}$, which is an $O(n)$ operation due to $\mathbf{W} \in \mathbb{R}^{n \times r}$ having sparse rows. Next, we apply $\mathbf{A}(\mathbf{W}^\top\mathbf{x})$. Since \mathbf{A} is a Toeplitz matrix, this is $O(r \log r)$ as per Section 3.1. Finally, $\mathbf{W}(\mathbf{A}\mathbf{W}^\top\mathbf{x})$, the action of \mathbf{W} , is again an $O(n)$ operation. Thus computing $\tilde{\mathbf{T}}\mathbf{x}$ is $O(n + r \log r)$ computation. On a GPU, this factorization achieves a speedup from having small r and being able to leverage efficient parallelized matrix multiplication on specialized hardware. However, in PyTorch [32], we note that for medium sized matrices up to $n = 512$, the time required for data movement in order to perform sparse-dense matrix multiplications can be higher than that of simply performing dense matrix multiplication. This means that in practice, we may instead choose to perform batched dense matrix multiplication, which yields an absolute speedup but a worse asymptotic complexity of $O(nr^2 + r \log r)$.

3.2.2 Inverse Time Warp

TNNs use $k_l(i - j) = \lambda^{|i-j|} \text{RPE}_l(i - j)$, where $\text{RPE}_l(i - j)$ is an MLP. There are two issues: 1) the sequential computations required for an MLP are slow, and we only need to evaluate at $2r - 1$ points using SKI instead of $2n - 1$ to produce the full matrix; 2) extrapolation is used in extending to longer sequence lengths than the MLP was trained on, which is generally less reliable than interpolation.

In Proposition 1, we note that an MLP $f : \mathbb{R} \rightarrow \mathbb{R}^d$ with ReLU activations and layer normalization is d piecewise linear functions. Since we only need to evaluate at $2r - 1$ points, we could have RPE_l be a piecewise linear function with r grid points. However, we still need to handle extrapolation. One way to do this is via an inverse time warp. We let RPE_l linearly interpolate on $[-1, 1]$ with the constraint $\text{RPE}_l(0) = 0$ and define $x(t) = \text{sign}(t)\lambda^{|t|}$ for some $0 < \lambda < 1$. We then let

$$k_l(i - j) = \text{RPE}_l(x(i - j)).$$

3.3 Causal Training

The SKI approach was appealing as it allowed for training bidirectional TNNs with linear complexity. However, fast causal masking negates SKI’s benefits: we show this in Appendix B. Thus we need an alternate speedup in the causal case. We propose using an MLP in the Fourier domain to avoid explicitly applying a decay bias in time domain, and use the Hilbert transform to enforce causality. We now describe how we can learn a causal kernel when working in frequency domain. We first define the discrete Hilbert transform, the key tool for achieving this.

Definition 1. The *discrete Hilbert transform* of the discrete Fourier transform \hat{k} is given by

$$\mathcal{H}\{\hat{k}\} = \hat{k} * h$$

where $*$ denotes convolution and

$$h[l] = \begin{cases} 0, & l \text{ even} \\ \frac{2}{\pi i}, & l \text{ odd} \end{cases}$$

The real and imaginary parts of the Fourier transform of a causal function are related to each other through the Hilbert transform. Thus, in order to represent a causal signal, we can model only the real part and compute the corresponding imaginary part. That is, we first estimate an even real function \hat{k} (symmetric about 0) using an MLP. We then take

$$\hat{k}_{\text{causal}}(\omega) = \hat{k}(\omega) - i\mathcal{H}\{\hat{k}\}(\omega)$$

The inverse Fourier transform k_{causal} of \hat{k}_{causal} will thus be causal. For a discussion of why this ensures causality, see [33]. See Algorithm 2 for TNO pseudocode using this approach. Different choices for the smoothness of the frequency domain MLP will lead to different decay rates in time domain, so that smoothness in frequency domain essentially serves the same purpose as the decay bias in [1]. We discuss this theoretically in Section 4.2. Note that we also find that working directly in the frequency domain for bidirectional models (without the Hilbert transform) is often competitive with SKI for speed (despite being $O(n \log n)$ instead of $O(n + r \log r)$) due to needing one fewer FFT.

Algorithm 2 Causal TNO via Discrete Hilbert Transform

Given sequence $\mathbf{X} \in \mathbb{R}^{n \times d}$ with columns \mathbf{x}^l
Hyperparameters activation function
for $l = 1, \dots, d$ **do**
 $\hat{\mathbf{x}}^l \leftarrow \mathcal{F}\{\mathbf{x}^l\}$, where \mathcal{F} is the rFFT.
 Compute even real function $\hat{k}^l = \text{RPE}_l(\omega)$, $\omega = \frac{m\pi}{n}$, $m = 0, \dots, n$.
 Take discrete Hilbert transform $\mathcal{H}\{\hat{k}^l\}$ via the rFFT and irFFT.
 Compute $\hat{k}_{\text{causal}}^l(\omega) = \hat{k}^l(\omega) - i\mathcal{H}\{\hat{k}^l\}(\omega)$ for $\omega = \frac{m\pi}{n}$, $m = 0, \dots, n$.
 $\mathbf{y}^l \leftarrow \mathcal{F}^{-1}\{\hat{k}_{\text{causal}}^l \odot \hat{\mathbf{x}}^l\}$, where \mathcal{F}^{-1} is the irFFT and \odot denotes an element-wise product.
end for
Return $\text{TNO}(\mathbf{X}) = (\mathbf{y}^1, \dots, \mathbf{y}^d)$

4 Theory

We show in Proposition 1 that an MLP mapping from scalars with layer norm and ReLU activations is piecewise linear and continuous, suggesting that using an MLP that we only need to evaluate at a small number of points may be overparametrized, justifying the use of interpolated piecewise linear functions. In section 4.1 we analyze the spectral norm of the matrix approximation error for SKI. We assume the sparse component is exactly identifiable and bound the error of approximating the smooth term via a low-rank SKI factorization. We leave the problem of relaxing this assumption to future work. In section 4.2, we analyze how by using different activations with different smoothness when learning the DTFT of the kernel, we obtain corresponding decay rates for the time domain signal.

Proposition 1. A ReLU MLP $f : \mathbb{R} \rightarrow \mathbb{R}^d$ with layer norm and no activation on its output is d piecewise linear continuous functions.

Proof. See Appendix C. □

4.1 Matrix Approximation Spectral Norm Error

We give our main error bound for our SKI based low rank approximation. Note that this requires that our kernel is $N + 1$ times continuously differentiable, while the kernel we use in practice uses a piecewise linear function and is thus non-differentiable. In theory, we would need a smoother kernel, adding additional computation overhead. However, we find that empirical performance is still quite strong and thus we simply use piecewise linear kernels but include the error bound for completeness. Our results depends on the Nyström error \mathbf{E}_{nystr} : its l^2 norm is bounded in [16].

Theorem 1. *Assume that \mathbf{A} is non-singular and $k : [p_1, p_r] \rightarrow \mathbb{R}$ is an $N + 1$ times continuously differentiable function, where p_1 is the smallest inducing point and p_r is the largest. Let $\mathbf{T}_{r,opt}$ be the optimal rank r approximation to \mathbf{T} and let*

$$\mathbf{E}_{SKI} = \mathbf{WAW}^\top - \mathbf{T}_{r,opt}$$

be the difference between the SKI approximation using linear interpolation and the optimal one, while

$$\mathbf{E}_{nystr} = \mathbf{FA}^{-1}\mathbf{B} - \mathbf{T}_{r,opt}$$

is the difference between the Nyström approximation and the optimal one. Then

$$\|\mathbf{E}_{SKI}\|_2 \leq \sqrt{nr} \max_{p_{n_1} \leq i \leq p_{n_N}} \frac{|\psi_N(i)|}{(N+1)!} L \left((N+1)\sqrt{n} + \frac{\min(\sigma_1(\mathbf{F}), \sigma_1(\mathbf{B}))}{\sigma_r(\mathbf{A})} \right) + \|\mathbf{E}_{nystr}\|_2.$$

where $\psi_N(i) = \prod_{j=1}^N (i - p_{n_j})$ with p_{n_j} being the j th closest inducing point to i , L is an upper bound on the $N + 1$ th derivative of k , and $\sigma_i(\mathbf{M})$ denotes the i th largest singular value of matrix \mathbf{M} .

Proof. See Appendix D.1. □

For linear interpolation $\frac{|\psi_N(i)|}{(N+1)!} \leq \frac{h^2}{8}$, where h is the spacing between two neighboring inducing points. We have considered the sparse component of the Toeplitz matrix to be identifiable and focused on the error of approximating the smooth component. While there are potential approaches to relaxing this assumption [34, 35, 36, 37, 38, 39, 40], they must be adapted properly to the Toeplitz setting. Thus, this additional analysis is outside the scope of this paper and a fruitful direction for future work.

4.2 Smoothness in Fourier Domain Implies Decay in Time Domain

We now discuss activation function choices when directly learning the discrete time Fourier transform (DTFT) \hat{k} as an MLP. In practice, we sample the DTFT to obtain the actually computable discrete Fourier transform (DFT) by evaluating the MLP with uniform spacing. Different levels of smoothness of the MLP \hat{k} imply different decay rates of the signal k . One can think of the choice of activation function as a parametric form for the decay bias. For an MLP, using a GeLU activation implies super-exponential time domain decay. Using SiLU implies super-polynomial time domain decay. For ReLU the signal is square summable. While this subsection focuses on the theoretical relationship between smoothness and decay, in Appendix E.3 we show visualizations demonstrating that these relationships are observed in practice. We first define the DTFT and its inverse.

Definition 2. *The discrete time Fourier transform [41, 33] \hat{k} or $\mathcal{F}\{k\}$ of k is given by*

$$\hat{k}(\omega) = \sum_{m=-\infty}^{\infty} k[m] \exp(-i\omega m)$$

Definition 3. *The inverse discrete time Fourier transform of the DTFT \hat{k} is given by*

$$\mathcal{F}^{-1}\{\hat{k}\}[n] = \frac{1}{2\pi} \int_{-\pi}^{\pi} \hat{k}(\omega) \exp(i\omega n) d\omega$$

We now give three theorems relating smoothness of the DTFT to decay of the signal (its inverse).

Theorem 2. *If we use a GeLU MLP for the DTFT \hat{k} , then the signal $k[n]$ will have decay*

$$k[n] = O(\exp(-an))$$

for all $a > 0$.

Proof. See Appendix E.1. □

Theorem 3. *If we use a SiLU MLP for the DTFT \hat{k} , then the signal $k[n]$ will have decay*

$$|k[n]| \leq \frac{1}{2\pi|n|^N} \|\hat{k}^{(N)}\|_1$$

for all $n \neq 0, N \in \mathbb{N}$.

Proof. See Appendix E.2. □

Theorem 4. *If we use a ReLU MLP for the DTFT \hat{k} then $\|k\|_2 < \infty$ (the signal is square summable).*

Proof. Note that $\hat{k} \in L^2[-\pi, \pi]$ since it is continuous. Then apply Parseval’s theorem. □

5 Experiments

We perform experiments in two areas: pre-training a causal language model on Wikitext-103 [8] and training bidirectional models on Long-Range Arena. We start with the repositories of the TNN paper² and use their training and hyper-parameter settings unless indicated otherwise. We use Lambda cloud hardware, where we used three 8x A100 and two 8x V100 instances, as well as a handful of 1x A100 instances for preliminary research. We also used a 1x A6000 on vast.ai for the timing experiments so that we controlled hardware to match [1].

5.1 Pre-training a Causal Language Model

We aim to predict the next word, conditional on a fixed length sequence of previous words. Table 1 compares FD-TNN’s pre-training perplexity [8] to existing models: it almost exactly matches that of TNNs. Our approach is faster for the same capacity: at sequence length 512 with 6 layer RPEs (as in the TNN paper), FD TNN is 15% faster than the baseline TNN on a single A100 GPU. When both use a three layer RPE, FD TNN is 10% faster. We provide some additional details for this experiment as well as for bidirectional pre-training using FD-TNN (we see larger speed gains) in Appendix F.1.1.

5.2 Long-Range Arena

The Long-Range Arena (LRA) is a benchmark with several long sequence datasets. The goal is to achieve both high LRA score (predictive performance) and training steps per second. Following [1], we take the TNN architecture and their tuned hyperparameter (HP) configurations³, simply replacing their TNO module with our SKI-TNO module with $r = 64$ and $m = 32$. We use $\lambda = 0.99$ where they set $\lambda = 1$, but otherwise perform *no additional HP tuning* on 1D tasks and use smaller layers for the 2D tasks. This is in fact to our detriment: we could potentially achieve even higher accuracy with tuning. We select the checkpoint with the highest validation accuracy and report the corresponding test accuracy. We achieve the second highest average accuracy at this size, second only to TNN. We show our results in Table 2.

²<https://github.com/OpenNLP/tnn>

³<https://github.com/OpenNLP/lra>

Architecture	PPL (val)	PPL (test)	Params (m)
(Attn-based)			
Trans	24.40	24.78	44.65
LS	23.56	24.05	47.89
Flash	25.92	26.70	42.17
1+elu	27.44	28.05	44.65
Performer	62.50	63.16	44.65
Cosformer	26.53	27.06	44.65
(MLP-based)			
Syn(D)	31.31	32.43	46.75
Syn(R)	33.68	34.78	44.65
gMLP	28.08	29.13	47.83
(SS-based)			
S4	38.34	39.66	45.69
DSS	39.39	41.07	45.73
GSS	29.61	30.74	43.84
(TNN-based)			
TNN (reproduced, 3 layers)	23.98 (23.96)	24.67 (24.61)	48.68 (48.59)
FD-TNN: Ours, 3 layers	23.97	24.56	48.58

Table 1: **Performance on Wikitext-103, Causal Language Model.** We reproduce [1]’s table except for the bottom two rows corresponding to the baseline TNN and our FD-TNN. For both we use the same RPE config with 3 layers. We add in parenthesis the baseline TNN results that we reproduced. We have nearly the same perplexity as the baseline TNN. Our approach is faster: at sequence length 512 with a six layer RPE (as in the TNN paper), FD TNN is 15% faster than the baseline TNN. For a three layer RPE, it is 10% faster.

Architecture	Text	ListOps	Retrieval	Pathfinder	Image	Avg
TNN	86.39	47.33	89.40	73.89	77.84	74.97
SKI-TNN	83.19	45.31	88.73	68.30	76.46	72.40
FD-TNN	85.00	55.21	90.26	69.45	84.12	72.92

Table 2: **Performance on Long Range Arena.** We reproduce experiments and train our proposed variants using tuned hyperparameters from [1]. Our proposed SKI-TNN and FD-TNN achieve similar overall performance with *no additional hyperparameter tuning* on 1D LRA tasks and a small amount of tuning on 2D tasks.

6 Conclusion

In this paper, we note that [1]’s Toeplitz neural networks essentially apply the action of a generalized Gram matrix (the Toeplitz matrix) for an asymmetric kernel (the RPE times decay bias) as their main computationally expensive operation. The visualized learned Gram matrices motivate a sparse and low rank decomposition. We thus propose two different approaches to improve efficiency. In the bidirectional setting, we extend SKI to the asymmetric setting and use linear interpolation over a small set of inducing points to avoid the MLP entirely, while using an inverse time warp to handle extrapolation to time points not observed during training. This approach reduces the mathematical complexity from $O(n \log n)$ to $O(n + r \log r)$, where r is the number of inducing points. However in practice, we do not actually use $O(n + r \log r)$ code due to a reshape required for sparse tensors leading them actually being *slower* than dense tensors. Thus we actually use $O(nr^2 + r \log r)$ in code: still much faster than Vanilla TNN for small r . For causal training, as causal masking negates SKI’s benefits, we instead eliminate the explicit decay bias. We do this by working directly in the frequency domain, enforcing causality via the Hilbert transform and enforcing decay in time domain via smoothness. For the bidirectional case, we eliminate the FFT applied to the kernels. While this maintains $O(n \log n)$ computational complexity, it leads to a substantial speedup in practice. Overall, we outperform TNNs on speed with minimal predictive performance degradation.

References

- [1] Zhen Qin, Xiaodong Han, Weixuan Sun, Bowen He, Dong Li, Dongxu Li, Yuchao Dai, Lingpeng Kong, and Yiran Zhong. Toeplitz neural network for sequence modeling. In The Eleventh International Conference on Learning Representations, 2023.
- [2] Andrew Wilson and Hannes Nickisch. Kernel interpolation for scalable structured Gaussian processes (KISS-GP). In International conference on machine learning, pages 1775–1784. PMLR, 2015.
- [3] Angelos Katharopoulos, Apoorv Vyas, Nikolaos Pappas, and François Fleuret. Transformers are RNNs: Fast autoregressive transformers with linear attention. In International Conference on Machine Learning, pages 5156–5165. PMLR, 2020.
- [4] Yi Tay, Mostafa Dehghani, Samira Abnar, Yikang Shen, Dara Bahri, Philip Pham, Jinfeng Rao, Liu Yang, Sebastian Ruder, and Donald Metzler. Long Range Arena: A Benchmark for Efficient Transformers. In International Conference on Learning Representations, 2020.
- [5] Ashish Vaswani, Noam Shazeer, Niki Parmar, Jakob Uszkoreit, Llion Jones, Aidan N Gomez, Łukasz Kaiser, and Illia Polosukhin. Attention is all you need. Advances in neural information processing systems, 30, 2017.
- [6] Jordan Hoffmann, Sebastian Borgeaud, Arthur Mensch, Elena Buchatskaya, Trevor Cai, Eliza Rutherford, Diego de las Casas, Lisa Anne Hendricks, Johannes Welbl, Aidan Clark, Tom Hennigan, Eric Noland, Katherine Millican, George van den Driessche, Bogdan Damoc, Aurelia Guy, Simon Osindero, Karen Simonyan, Erich Elsen, Oriol Vinyals, Jack William Rae, and Laurent Sifre. An empirical analysis of compute-optimal large language model training. In Alice H. Oh, Alekh Agarwal, Danielle Belgrave, and Kyunghyun Cho, editors, Advances in Neural Information Processing Systems, 2022.
- [7] Kevin Clark, Minh-Thang Luong, Quoc V. Le, and Christopher D. Manning. Electra: Pre-training text encoders as discriminators rather than generators. In International Conference on Learning Representations, 2020.
- [8] Stephen Merity, Caiming Xiong, James Bradbury, and Richard Socher. Pointer Sentinel Mixture Models. In International Conference on Learning Representations, 2016.
- [9] Alex Wang, Amanpreet Singh, Julian Michael, Felix Hill, Omer Levy, and Samuel R Bowman. Glue: A multi-task benchmark and analysis platform for natural language understanding. In International Conference on Learning Representations.
- [10] Yi Tay, Mostafa Dehghani, Dara Bahri, and Donald Metzler. Efficient transformers: A survey. ACM Computing Surveys, 55(6):1–28, 2022.
- [11] Shengjie Luo, Shanda Li, Tianle Cai, Di He, Dinglan Peng, Shuxin Zheng, Guolin Ke, Liwei Wang, and Tie-Yan Liu. Stable, fast and accurate: Kernelized attention with relative positional encoding. Advances in Neural Information Processing Systems, 34:22795–22807, 2021.
- [12] Michael Poli, Stefano Massaroli, Eric Nguyen, Daniel Y Fu, Tri Dao, Stephen Baccus, Yoshua Bengio, Stefano Ermon, and Christopher Ré. Hyena Hierarchy: Towards Larger Convolutional Language Models. arXiv preprint arXiv:2302.10866, 2023.
- [13] Evert J Nyström. Über die praktische auflösung von integralgleichungen mit anwendungen auf randwertaufgaben. Acta Mathematica, 54(1):185–204, 1930.
- [14] Christopher TH Baker. The numerical treatment of integral equations. Oxford University Press, 1977.
- [15] Yunyang Xiong, Zhanpeng Zeng, Rudrasis Chakraborty, Mingxing Tan, Glenn Fung, Yin Li, and Vikas Singh. Nyströmformer: A nyström-based algorithm for approximating self-attention. In Proceedings of the AAAI Conference on Artificial Intelligence, volume 35, pages 14138–14148, 2021.

- [16] Arik Nemtsov, Amir Averbuch, and Alon Schlar. Matrix compression using the Nyström method. Intelligent Data Analysis, 20(5):997–1019, 2016.
- [17] Yifan Chen, Qi Zeng, Heng Ji, and Yun Yang. Skyformer: Remodel self-attention with gaussian kernel and nyström method. Advances in Neural Information Processing Systems, 34:2122–2135, 2021.
- [18] H Peng, N Pappas, D Yogatama, R Schwartz, N Smith, and L Kong. Random Feature Attention. In International Conference on Learning Representations, 2021.
- [19] Krzysztof Marcin Choromanski, Valerii Likhoshesterov, David Dohan, Xingyou Song, Andreea Gane, Tamas Sarlos, Peter Hawkins, Jared Quincy Davis, Afroz Mohiuddin, Lukasz Kaiser, et al. Rethinking Attention with Performers. In International Conference on Learning Representations, 2021.
- [20] Ali Rahimi and Benjamin Recht. Random features for large-scale kernel machines. Advances in neural information processing systems, 20:1177–1184, 2007.
- [21] Rewon Child, Scott Gray, Alec Radford, and Ilya Sutskever. Generating long sequences with sparse transformers. arXiv preprint arXiv:1904.10509, 2019.
- [22] Tom Brown, Benjamin Mann, Nick Ryder, Melanie Subbiah, Jared D Kaplan, Prafulla Dhariwal, Arvind Neelakantan, Pranav Shyam, Girish Sastry, Amanda Askell, et al. Language models are few-shot learners. Advances in neural information processing systems, 33:1877–1901, 2020.
- [23] Manzil Zaheer, Guru Guruganesh, Kumar Avinava Dubey, Joshua Ainslie, Chris Alberti, Santiago Ontanon, Philip Pham, Anirudh Ravula, Qifan Wang, Li Yang, et al. Big Bird: Transformers for Longer Sequences. Advances in neural information processing systems, 33:17283–17297, 2020.
- [24] Albert Gu, Karan Goel, and Christopher Re. Efficiently modeling long sequences with structured state spaces. In International Conference on Learning Representations.
- [25] Jimmy T.H. Smith, Andrew Warrington, and Scott Linderman. Simplified state space layers for sequence modeling. In The Eleventh International Conference on Learning Representations, 2023.
- [26] Tri Dao, Daniel Y Fu, Khaled K Saab, Armin W Thomas, Atri Rudra, and Christopher Ré. Hungry hungry hippos: Towards language modeling with state space models. arXiv preprint arXiv:2212.14052, 2022.
- [27] David W Romero, Anna Kuzina, Erik J Bekkers, Jakub Mikolaj Tomczak, and Mark Hoogendoorn. Ckconv: Continuous kernel convolution for sequential data. In International Conference on Learning Representations.
- [28] Daniel Y Fu, Elliot L Epstein, Eric Nguyen, Armin W Thomas, Michael Zhang, Tri Dao, Atri Rudra, and Christopher Ré. Simple hardware-efficient long convolutions for sequence modeling. arXiv preprint arXiv:2302.06646, 2023.
- [29] Xuezhe Ma, Chunting Zhou, Xiang Kong, Junxian He, Liangke Gui, Graham Neubig, Jonathan May, and Luke Zettlemoyer. Mega: Moving average equipped gated attention. In The Eleventh International Conference on Learning Representations, 2023.
- [30] Ruslan Khalitov, Tong Yu, Lei Cheng, and Zhirong Yang. Chordmixer: A scalable neural attention model for sequences with different length. In The Eleventh International Conference on Learning Representations, 2023.
- [31] Noam Shazeer. Glu variants improve transformer. arXiv preprint arXiv:2002.05202, 2020.
- [32] Adam Paszke, Sam Gross, Francisco Massa, Adam Lerer, James Bradbury, Gregory Chanan, Trevor Killeen, Zeming Lin, Natalia Gimelshein, Luca Antiga, et al. Pytorch: An imperative style, high-performance deep learning library. Advances in neural information processing systems, 32, 2019.

- [33] Alan V Oppenheim and Schafer R W. Discrete Time Signal Processing. Prentice-Hall, 2010.
- [34] Benjamin Recht, Maryam Fazel, and Pablo A Parrilo. Guaranteed minimum-rank solutions of linear matrix equations via nuclear norm minimization. SIAM review, 52(3):471–501, 2010.
- [35] Emmanuel J Candes and Yaniv Plan. Matrix completion with noise. Proceedings of the IEEE, 98(6):925–936, 2010.
- [36] Tianyi Zhou and Dacheng Tao. Godec: Randomized low-rank & sparse matrix decomposition in noisy case. In Proceedings of the 28th International Conference on Machine Learning, 2011.
- [37] Jonathan Mei and José M F Moura. SILVar: Single Index Latent Variable Models. IEEE Transactions on Signal Processing, 66:2790 – 2803, 3 2018.
- [38] Venkat Chandrasekaran, Sujay Sanghavi, Pablo A Parrilo, and Alan S Willsky. Rank-sparsity incoherence for matrix decomposition. SIAM Journal on Optimization, 21(2):572–596, 2011.
- [39] Venkat Chandrasekaran, Pablo A. Parrilo, and Alan S. Willsky. Latent variable graphical model selection via convex optimization. Ann. Stat., 40:1935–1967, 8 2012.
- [40] Teng Zhang and Yi Yang. Robust PCA by manifold optimization. The Journal of Machine Learning Research, 19(1):3101–3139, 2018.
- [41] John G Proakis and Dimitris G Manolakis. Introduction to digital signal processing. Prentice Hall Professional Technical Reference, 1988.
- [42] Jeffrey Wong. Math 563 lecture notes, polynomial interpolation: the fundamentals, 2020. URL:<https://services.math.duke.edu/~jtwong/math563-2020/lectures/Lec1-polyinterp.pdf>.
- [43] Mhenni Benghorbal (https://math.stackexchange.com/users/35472/mhenni_benghorbal). How to prove error function erf is entire (i.e., analytic everywhere)? Mathematics Stack Exchange, 2017. URL:<https://math.stackexchange.com/q/203920> (version: 2017-04-13).
- [44] Christopher Heil. Introduction to Real Analysis, volume 280. Springer, 2019.

Appendix

Table of Contents

A	Toeplitz Neural Network Architecture Diagrams	13
B	Causal Masking negates SKI’s benefits	13
C	Proofs Related to Proposition 1	14
D	Proofs for Matrix Approximation Error Spectral Norm	14
D.1	Proof of Theorem 1	14
E	Smoothness and Decay	17
E.1	GeLU: Proofs Related to Theorem 5	17
E.2	SiLU: Proofs Related to Theorem 3	18
E.3	Visualizations for Smoothness and Decay	19
F	Experiment Details and Additional Results	19
F.1	Wikitext-103	19

A Toeplitz Neural Network Architecture Diagrams

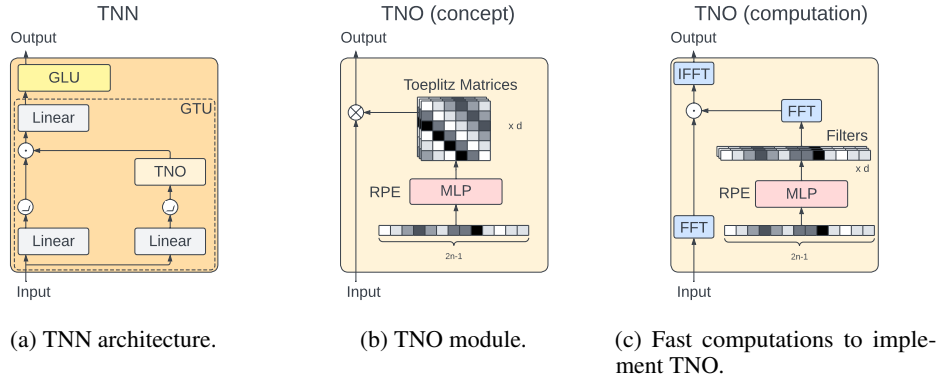


Figure 3: Toeplitz Neural Network and Toeplitz Neural Operators: (a) The overall architecture of a TNN layer [1]. (b) Conceptually, the TNO multiplies each channel of the input by a different Toeplitz matrix. (c) Computationally, the TNO uses FFT’s for speed.

B Causal Masking negates SKI’s benefits

We now show how requiring causal masking for SKI negates its computational benefits on popular hardware accelerators that optimize parallelized matrix multiplication, such as GPUs. Thus, we will need an alternative approach.

First, let’s examine the algorithm from [3]. Let $\mathbf{x}' = \mathbf{T}\mathbf{x}$, the subscripted $\mathbf{w}_i \in \mathbb{R}^r$ denote the i -th row of \mathbf{W} taken as a column vector, and the subscripted square bracketed $[\mathbf{W}]_i$ denote taking the

i -th row as a column. That is,

$$\begin{aligned} \mathbf{x}' &= (x'_1 \quad \dots \quad x'_n)^\top & \mathbf{W} &= (\mathbf{w}_1 \quad \dots \quad \mathbf{w}_n)^\top \\ \mathbf{x} &= (x_1 \quad \dots \quad x_n)^\top & [\mathbf{W}]_i &= \mathbf{w}_i. \end{aligned}$$

Then

$$x'_i = \sum_{j=1}^i \mathbf{w}_i^\top \mathbf{A} \mathbf{w}_j x_j$$

Let us define intermediate sums and resulting recursions,

$$\begin{aligned} \mathbf{s}_i &\triangleq \sum_{j=1}^i \mathbf{w}_j x_j \in \mathbb{R}^r & \mathbf{s}'_i &\triangleq \sum_{j=1}^i \mathbf{A} \mathbf{w}_j x_j \in \mathbb{R}^r \\ \Rightarrow \mathbf{s}_{i+1} &= \mathbf{s}_i + \mathbf{w}_{i+1} x_{i+1} & \Rightarrow \mathbf{s}'_{i+1} &= \mathbf{s}'_i + \mathbf{A} \mathbf{w}_{i+1} x_{i+1} \end{aligned}$$

so that

$$x'_i = \mathbf{w}_i^\top \mathbf{s}'_i = \mathbf{w}_i^\top \mathbf{A} \mathbf{s}_i = [\mathbf{W} \mathbf{A}]_i^\top \mathbf{s}_i.$$

While we *want* to apply the action of \mathbf{A} to $\mathbf{W}^\top \mathbf{x} \in \mathbb{R}^r$ once, which takes $O(r \log r)$. Instead, we *have* to compute one of: (a) $\mathbf{A} \mathbf{s}_i \forall i = 1, \dots, n$; (b) $\mathbf{W} \mathbf{A}$; or (c) $\mathbf{A} \mathbf{W}^\top$; all of which take at least $O(nr)$. However, that is not even the largest practical loss. Instead, it is the fact that both cumulative sums \mathbf{s}_i and \mathbf{s}'_i are sequential in nature to compute efficiently (it *is* possible to parallelize the computation with $O(n^2 r)$ memory complexity, also defeating the purpose of this exercise). We found that the sequential nature of the cumulative sum makes it slower than the baseline TNN with FFTs in practice for moderate sequence lengths of at least up to 2048 on current GPUs (NVidia V100, A10, A100). Thus, we need to find an alternate approach for the causal setting.

C Proofs Related to Proposition 1

We first introduce two auxiliary lemmas, and then prove our main result, which follows immediately from the auxiliary lemmas.

Lemma 1. *A ReLU MLP $f : \mathbb{R} \rightarrow \mathbb{R}$ with no activation on its output is piecewise linear continuous.*

Proof. Each pre-activation node is a linear combination of piecewise linear continuous functions, and is thus piecewise linear continuous. Each activation applies ReLU, which is piecewise linear and the composition of piecewise linear continuous functions is also piecewise linear continuous. The output is a pre-activation and is thus piecewise linear continuous. \square

Lemma 2. *Adding layer normalization to a ReLU MLP $f : \mathbb{R} \rightarrow \mathbb{R}$ preserves piecewise linearity.*

Proof. Layer normalization applies the same affine transformation to each node in a layer. Since an affine transformation of a piecewise linear continuous function is still piecewise linear continuous, adding layer normalization to an MLP preserves piecewise linear continuity. \square

Proposition 1. *A ReLU MLP $f : \mathbb{R} \rightarrow \mathbb{R}^d$ with layer norm and no activation on its output is d piecewise linear continuous functions.*

Proof. Follows immediately from Lemmas 1 and 2. \square

D Proofs for Matrix Approximation Error Spectral Norm

D.1 Proof of Theorem 1

Theorem 1. *Assume that \mathbf{A} is non-singular and $k : [p_1, p_r] \rightarrow \mathbb{R}$ is an $N + 1$ times continuously differentiable function, where p_1 is the smallest inducing point and p_r is the largest. Let $\mathbf{T}_{r, \text{opt}}$ be the optimal rank r approximation to \mathbf{T} and let*

$$\mathbf{E}_{SKI} = \mathbf{W} \mathbf{A} \mathbf{W}^\top - \mathbf{T}_{r, \text{opt}}$$

be the difference between the SKI approximation using linear interpolation and the optimal one, while

$$\mathbf{E}_{nyst} = \mathbf{F}\mathbf{A}^{-1}\mathbf{B} - \mathbf{T}_{r,opt}$$

is the difference between the Nyström approximation and the optimal one. Then

$$\|\mathbf{E}_{SKI}\|_2 \leq \sqrt{nr} \max_{p_{n_1} \leq i \leq p_{n_N}} \frac{|\psi_N(i)|}{(N+1)!} L \left((N+1)\sqrt{n} + \frac{\min(\sigma_1(\mathbf{F}), \sigma_1(\mathbf{B}))}{\sigma_r(\mathbf{A})} \right) + \|\mathbf{E}_{nyst}\|_2.$$

where $\psi_N(i) = \prod_{j=1}^N (i - p_{n_j})$ with p_{n_j} being the j th closest inducing point to i , L is an upper bound on the $N+1$ th derivative of k , and $\sigma_i(\mathbf{M})$ denotes the i th largest singular value of matrix \mathbf{M} .

Proof. We first decompose the difference between the SKI approximation and the optimal rank r approximation into the sum of two terms: the difference between the SKI and the Nyström approximations, and the difference between the Nyström and optimal rank r approximations.

$$\begin{aligned} \mathbf{E}_{SKI} &= \mathbf{W}\mathbf{A}\mathbf{W}^\top - \mathbf{T}_{r,opt} \\ &= \mathbf{W}\mathbf{A}\mathbf{W}^\top - \mathbf{F}\mathbf{A}^{-1}\mathbf{B} + \mathbf{F}\mathbf{A}^{-1}\mathbf{B} - \mathbf{T}_{r,opt} \\ &= \mathbf{W}\mathbf{A}\mathbf{W}^\top - \mathbf{F}\mathbf{A}^{-1}\mathbf{B} + \mathbf{E}_{nyst} \end{aligned}$$

so that

$$\|\mathbf{E}_{SKI}\|_2 \leq \|\mathbf{W}\mathbf{A}\mathbf{W}^\top - \mathbf{F}\mathbf{A}^{-1}\mathbf{B}\|_2 + \|\mathbf{E}_{nyst}\|_2$$

We need to bound $\|\mathbf{W}\mathbf{A}\mathbf{W}^\top - \mathbf{F}\mathbf{A}^{-1}\mathbf{B}\|_2$, the operator norm of the difference between the SKI and the Nyström approximations.

$$\begin{aligned} &\|\mathbf{W}\mathbf{A}\mathbf{A}^{-1}\mathbf{A}\mathbf{W}^\top - \mathbf{F}\mathbf{A}^{-1}\mathbf{B}\|_2 \\ &= \|\mathbf{W}\mathbf{A}\mathbf{A}^{-1}\mathbf{A}\mathbf{W}^\top - \mathbf{F}\mathbf{A}^{-1}\mathbf{A}\mathbf{W}^\top + \mathbf{F}\mathbf{A}^{-1}\mathbf{A}\mathbf{W}^\top - \mathbf{F}\mathbf{A}^{-1}\mathbf{B}\|_2 \\ &\leq \|\mathbf{W}\mathbf{A} - \mathbf{F}\|_2 \|\mathbf{W}^\top\|_2 + \|\mathbf{F}\mathbf{A}^{-1}\|_2 \|\mathbf{A}\mathbf{W}^\top - \mathbf{B}\|_2 \\ &\leq \sigma_1(\mathbf{W}) \|\mathbf{W}\mathbf{A} - \mathbf{F}\|_2 + \frac{\sigma_1(\mathbf{F})}{\sigma_r(\mathbf{A})} \|\mathbf{A}\mathbf{W}^\top - \mathbf{B}\|_2. \end{aligned} \quad (1)$$

The first term describes the error due to approximation of \mathbf{F} , the left Nyström factor, while the second term describes the error due to approximation of \mathbf{B} , the right one. We can use standard interpolation results to bound $\|\mathbf{W}\mathbf{A} - \mathbf{F}\|_2$ and $\|\mathbf{A}\mathbf{W}^\top - \mathbf{B}\|_2$. Recall that the left Nyström factor and inducing Gram matrix have terms

$$\begin{aligned} \mathbf{F}_{ij} &= k(i, p_j) \\ \mathbf{A}_{ij} &= k(p_i, p_j), \end{aligned}$$

so that $(\mathbf{W}\mathbf{A})_{ij} = \tilde{k}(i, p_j)$ approximates $\mathbf{F}_{ij} = k(i, p_j)$ using interpolation. For linear interpolation this is

$$\tilde{k}(i, p_j) = w_i k(p_A, p_j) + (1 - w_i) k(p_B, p_j).$$

where p_A, p_B are the two closest inducing points to i . More generally with polynomial interpolation of degree N we use p_{n_1}, \dots, p_{n_N} to denote the N closest inducing points to i . Using the Lagrange error formula, polynomial interpolation has the following error bound [42]

$$|\tilde{k}(i, p_j) - k(i, p_j)| \leq \left| \frac{\psi_N(i)}{(N+1)!} \right| \max_{p_{n_1} \leq x \leq p_{n_N}} \left| \frac{\partial^{N+1}}{\partial x^{N+1}} k(x, p_j) \right|$$

where $\psi_N(i) = \prod_{j=1}^N (i - p_{n_j})$. As an example, for linear interpolation this gives

$$\begin{aligned} |\tilde{k}(i, p_j) - k(i, p_j)| &\leq \left| \frac{(i - p_A)(i - p_B)}{2} \right| \max_{p_A \leq x \leq p_B} \left| \frac{\partial^2}{\partial x^2} k(x, p_j) \right| \\ &\leq \frac{h^2}{8} \max_{p_A \leq x \leq p_B} \left| \frac{\partial^2}{\partial x^2} k(x, p_j) \right|, \end{aligned}$$

where $h = p_B - p_A$ is the distance between any two neighboring inducing points. Note that we assumed the $N + 1$ th partial is continuous and since we are interested in k on a compact domain, the $N + 1$ th partial is bounded, say by L . Thus,

$$\begin{aligned} |\tilde{k}(i, p_j) - k(i, p_j)| &\leq \left| \frac{\psi_N(i)}{(N+1)!} \right| L \\ \Rightarrow (\tilde{k}(i, p_j) - k(i, p_j))^2 &\leq \left(\frac{\psi_N(i)}{(N+1)!} \right)^2 L^2 \end{aligned}$$

and thus we can bound the error in the Frobenius norm of the left factor's SKI approximation as

$$\begin{aligned} \|\mathbf{WA} - \mathbf{F}\|_F^2 &\leq nr \max_{p_{n_1} \leq i \leq p_{n_N}} \left(\frac{\psi_N(i)}{(N+1)!} \right)^2 L^2 \\ \Rightarrow \|\mathbf{WA} - \mathbf{F}\|_F &\leq \sqrt{nr} \max_{p_{n_1} \leq i \leq p_{n_N}} \frac{|\psi_N(i)|}{(N+1)!} L. \end{aligned}$$

This implies an operator norm bound

$$\begin{aligned} \|\mathbf{WA} - \mathbf{F}\|_2 &\leq \|\mathbf{WA} - \mathbf{F}\|_F \\ &\leq \sqrt{nr} \max_{p_{n_1} \leq i \leq p_{n_N}} \frac{|\psi_N(i)|}{(N+1)!} L. \end{aligned}$$

The right factor approximation $\|\mathbf{AW}^\top - \mathbf{B}\|_2$ has the same bound. Plugging into Eqn. 1, we have

$$\|\mathbf{WAA}^{-1}\mathbf{AW}^\top - \mathbf{FA}^{-1}\mathbf{B}\|_2 \leq \sqrt{nr} \max_{p_{n_1} \leq i \leq p_{n_N}} \frac{|\psi_N(i)|}{(N+1)!} L \left(\sigma_1(\mathbf{W}) + \frac{\sigma_1(\mathbf{F})}{\sigma_s(\mathbf{A})} \right)$$

which gives

$$\|\mathbf{E}_{SKI}\|_2 \leq \sqrt{nr} \max_{p_{n_1} \leq i \leq p_{n_N}} \frac{|\psi_N(i)|}{(N+1)!} L \left(\sigma_1(\mathbf{W}) + \frac{\sigma_1(\mathbf{F})}{\sigma_r(\mathbf{A})} \right) + \|\mathbf{E}_{nyst}\|_2.$$

Now recall that

$$\begin{aligned} \sigma_1(\mathbf{W}) &= \|\mathbf{W}\|_2 \\ &\leq \sqrt{n} \|\mathbf{W}\|_\infty \\ &\leq (N+1)\sqrt{n} \end{aligned}$$

since \mathbf{W} has at most $N + 1$ non-zero entries in each row, so that

$$\|\mathbf{E}_{SKI}\|_2 \leq \sqrt{nr} \max_{p_{n_1} \leq i \leq p_{n_N}} \frac{|\psi_N(i)|}{(N+1)!} L \left((N+1)\sqrt{n} + \frac{\sigma_1(\mathbf{F})}{\sigma_r(\mathbf{A})} \right) + \|\mathbf{E}_{nyst}\|_2.$$

Note that we could have alternatively expanded Eqn. 1 using terms based on \mathbf{B} instead of \mathbf{F} . This gives

$$\begin{aligned} &\|\mathbf{WAA}^{-1}\mathbf{AW}^\top - \mathbf{FA}^{-1}\mathbf{B}\|_2 \\ &= \|\mathbf{WAA}^{-1}\mathbf{AW}^\top - \mathbf{WAA}^{-1}\mathbf{B} + \mathbf{WAA}^{-1}\mathbf{B} - \mathbf{FA}^{-1}\mathbf{B}\|_2 \\ &\leq \|\mathbf{W}\|_2 \|\mathbf{AW}^\top - \mathbf{B}\|_2 + \|\mathbf{WA} - \mathbf{F}\|_2 \|\mathbf{A}^{-1}\mathbf{B}\|_2 \\ &\leq \sigma_1(\mathbf{W}) \|\mathbf{AW}^\top - \mathbf{B}\|_2 + \frac{\sigma_1(\mathbf{B})}{\sigma_r(\mathbf{A})} \|\mathbf{WA} - \mathbf{F}\|_2. \end{aligned} \tag{2}$$

Using Eqn. 2 instead of Eqn. 1 and taking the min of both results leads to a bound of

$$\|\mathbf{E}_{SKI}\|_2 \leq \sqrt{nr} \max_{p_{n_1} \leq i \leq p_{n_N}} \frac{|\psi_N(i)|}{(N+1)!} L \left((N+1)\sqrt{n} + \frac{\min(\sigma_1(\mathbf{F}), \sigma_1(\mathbf{B}))}{\sigma_r(\mathbf{A})} \right) + \|\mathbf{E}_{nyst}\|_2.$$

□

E Smoothness and Decay

E.1 GeLU: Proofs Related to Theorem 5

We analyze how modeling the DTFT with a GeLU MLP affects smoothness, the strongest form being an *entire* function, which is complex differentiable everywhere. We then analyze what this implies for the signal. We first recap three basic definitions from complex analysis. In Lemmas 3 and 4, we show GeLU MLPs are entire. In 2 we show that if a DTFT is entire then the signal will decay at faster than any exponential rate. Finally in Theorem 5, we show that modeling the DTFT with a GeLU MLP implies that the signal will decay faster than any exponential rate.

Definition 4. The *complex derivative* of $f : \mathbb{C} \rightarrow \mathbb{C}$ at $z_0 \in \mathbb{C}$ is defined as

$$f'(z_0) = \lim_{z \rightarrow z_0} \frac{f(z) - f(z_0)}{z - z_0}.$$

Definition 5. A function $f : \mathbb{C} \rightarrow \mathbb{C}$ is *holomorphic* at $z_0 \in \mathbb{C}$ if it is differentiable on a neighborhood of z_0 .

Definition 6. A function is *entire* if it is holomorphic on \mathbb{C} .

Lemma 3. The complex extension of the GeLU activation function is entire.

Proof. The GeLU activation function is $x\Phi(x)$, where $\Phi(x)$ is the standard normal CDF. The complex extension is thus $z\Phi(z)$. Recall that

$$\Phi(z) = \frac{1 + \text{Erf}(z/\sqrt{2})}{2}$$

where Erf is the error function. Clearly $z/\sqrt{2}$ is holomorphic on \mathbb{C} . It is well known that Erf is holomorphic on \mathbb{C} (see [43] for proof) and compositions of holomorphic functions are holomorphic. Thus $\Phi(z)$ is holomorphic. Finally, the product of holomorphic functions is holomorphic, so that $z\Phi(z)$ is. Since all of this was holomorphic on \mathbb{C} , the complex extension of the GeLU activation function is entire. \square

Lemma 4. Each output node of a GeLU MLP with layer norm is an entire function.

Proof. Linear combinations of holomorphic functions are holomorphic, as are compositions. Pre-activations are linear combinations and activations are compositions. The layer-norms are affine transformations, which are also holomorphic. Thus each output node is an entire function. \square

Proposition 2. If the DTFT is entire then

$$k[n] = O(\exp(-an))$$

for all $a > 0$.

Proof. Let's consider the Fourier series of $\hat{k}(-\omega)$, which is also entire. Its n th coefficient is given by

$$c_n = \frac{1}{2\pi} \int_{-\pi}^{\pi} \hat{k}(-\omega) \exp(-\omega in) d\omega.$$

Let $u = -\omega$; then $du = -d\omega$ and

$$\begin{aligned} c_n &= -\frac{1}{2\pi} \int_{-\pi}^{\pi} \hat{k}(u) \exp(uin) du \\ &= -k[n]. \end{aligned}$$

Now, Fourier series coefficients for analytic functions in a strip $[-a, a]$ decay as $O(\exp(-an))$. \square

Theorem 5. If we use a GeLU MLP for the DTFT \hat{k} , then the signal $k[n]$ will have decay

$$k[n] = O(\exp(-an))$$

for all $a > 0$.

Proof. Follows immediately from Lemma 4 and Proposition 2. \square

E.2 SiLU: Proofs Related to Theorem 3

We first argue in Lemma 5 that the SiLU activation function is C^∞ . We then show in Proposition 3 that SiLU MLPs with layer norm are C^∞ and have integrable derivatives on compact domains. Next in Lemma 6, we argue that for an integrable DTFT, its inverse is bounded by a term proportional to the integral of the DTFT. In Proposition 4, we use the previous lemma to show that the DTFT being N times differentiable implies a decay rate for the original signal. Finally, we prove our main result, that using a SiLU MLP to model a DTFT leads to faster than any polynomial rate in the time domain.

Lemma 5. *SiLU is C^∞ .*

Proof. The sigmoid function is C^∞ , as is the function x . The product of C^∞ functions is C^∞ . \square

Proposition 3. *A SiLU MLP mapping scalars to scalars with layer norm is C^∞ with integrable derivatives on $[-\pi, \pi]$.*

Proof. A SiLU MLP with layer norm involves finite linear combinations and finitely many compositions of C^∞ functions, and is thus C^∞ . Now any SiLU MLP on a bounded domain has bounded derivatives of all orders (since they are continuous on a bounded domain). Thus, all derivatives are integrable on $[-\pi, \pi]$. \square

Lemma 6. *If the DTFT $\hat{k} \in L^1[-\pi, \pi]$, then k is bounded and*

$$\|k\|_\infty \leq \frac{1}{2\pi} \|\hat{k}\|_1$$

Proof. This essentially follows the proof technique of Lemma 9.2.3 in [44], but in the reverse order and using the DTFT instead of the continuous Fourier transform. The idea is to express the signal as the inverse DTFT, which we can since $\hat{k} \in L^1[-\pi, \pi]$, and then use the fact that the values on the complex unit circle have magnitude 1.

$$\begin{aligned} |k[n]| &= \left| \frac{1}{2\pi} \int_{-\pi}^{\pi} \hat{k}(\omega) \exp(i\omega n) d\omega \right| \\ &\leq \frac{1}{2\pi} \int_{-\pi}^{\pi} |\hat{k}(\omega) \exp(i\omega n)| d\omega \\ &= \frac{1}{2\pi} \int_{-\pi}^{\pi} |\hat{k}(\omega)| d\omega \\ &= \frac{1}{2\pi} \|\hat{k}\|_1 \end{aligned}$$

\square

The next proposition describes how smoothness of the DTFT implies decay of a time domain signal. While there are many very related results in the literature (for instance, [44] shows the opposite direction for the continuous Fourier transform using a very similar proof technique), we were not able to find exactly this result stated or proven rigorously. Thus we state and prove it.

Proposition 4. *If the N th derivative of DTFT \hat{k} exists and is integrable on $[-\pi, \pi]$ then*

$$|k[n]| \leq \frac{1}{2\pi|n|^N} \|\hat{k}^{(N)}\|_1$$

for all $n \neq 0$.

Proof. We first take the derivative of the DTFT

$$\begin{aligned} \hat{k}(\omega) &= \sum_{m=-\infty}^{\infty} x[m] \exp(-i\omega m) \\ \hat{k}'(\omega) &= \frac{1}{i} \sum_{m=-\infty}^{\infty} mx[m] \exp(-i\omega m). \end{aligned}$$

Since \hat{k} is integrable over $[-\pi, \pi]$, we can plug it into the inverse DTFT

$$\begin{aligned} \frac{1}{2\pi} \int_{-\pi}^{\pi} \hat{k}'(\omega) \exp(i\omega n) d\omega &= \frac{1}{2\pi} \int_{-\pi}^{\pi} \frac{1}{i} \sum_{m=-\infty}^{\infty} mk[m] \exp(-i\omega m) \exp(i\omega n) d\omega \\ &= \frac{1}{i} \sum_{m=-\infty}^{\infty} mk[m] \delta[n - m] \\ &= \frac{n}{i} k[n] \end{aligned}$$

so that if \hat{k} and \hat{k}' are integrable, we obtain the key identity relating the inverse DTFTs of a DTFT and its derivative

$$\mathcal{F}^{-1}\{\hat{k}\} = \frac{i}{n} \mathcal{F}^{-1}\{\hat{k}'\}. \quad (3)$$

Thus

$$\begin{aligned} |k[n]| &\leq \frac{1}{|n|} \left| \mathcal{F}^{-1}\{\hat{k}'\}[n] \right| \\ &\leq \frac{1}{n^2} \left| \mathcal{F}^{-1}\{\hat{k}^{(2)}\}[n] \right| && \text{Eqn. 3, since } \hat{k}^{(2)} \text{ integrable} \\ &\leq \frac{1}{|n|^N} \left| \mathcal{F}^{-1}\{\hat{k}^{(N)}\}[n] \right| && \text{applying recursively, since } N\text{th derivative integrable} \\ &\leq \frac{1}{2\pi |n|^N} \|\hat{k}^{(N)}\|_1 \end{aligned}$$

where the last line follows from Lemma 6. □

Theorem 3. *If we use a SiLU MLP for the DTFT \hat{k} , then the signal $k[n]$ will have decay*

$$|k[n]| \leq \frac{1}{2\pi |n|^N} \|\hat{k}^{(N)}\|_1$$

for all $n \neq 0, N \in \mathbb{N}$.

Proof. This follows immediately from Proposition 3 and Proposition 4. □

E.3 Visualizations for Smoothness and Decay

We visualize the frequency responses and the corresponding impulse responses generated by the frequency domain (FD) RPE under the three activation functions for which we have shown theory, with results predicted by theory. For a randomly initialized FD RPE with Gelu activations the impulse responses decay to approximately 0 by $n = 30$: this is very rapid decay and the curves visually look like exponential decay. For a randomly initialized SiLU RPE, the resulting impulse responses are similar. For the ReLU case we show the generated filters from a trained FD TNN RPE from one of the TNN layers. We see the impulse responses visually decay to approximately 0 within the finite length of 512 points. This is a slower rate of decay than either of the previous two.

F Experiment Details and Additional Results

F.1 Wikitext-103

F.1.1 Fourier Domain

For both causal and bidirectional models we use the default model and training hyperparameters from the TNN repository as the TNN baseline, defined in the first two columns in [1] Table 13: LM (causal) and Roberta (bidirectional). One small HP discrepancy between the repository and table is the use of 7 decoder layers for the causal LM, which we used for all LM experiments, instead of the 6 they had in their paper. We find that we can reduce the default number of RPE layers from 6 to 3 and improve the speed of the baseline with slight quality improvements. We provide these reproduced perplexity

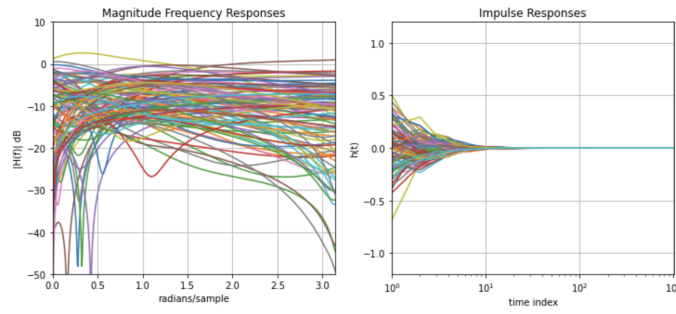


Figure 4: Frequency and impulse responses for a randomly initialized FD RPE MLP with **GeLU** activations. The curves on the left side are holomorphic, and theory predicts that the curves on the right hand will decay at faster than any exponential rate. They appear to decay approximately exponentially.

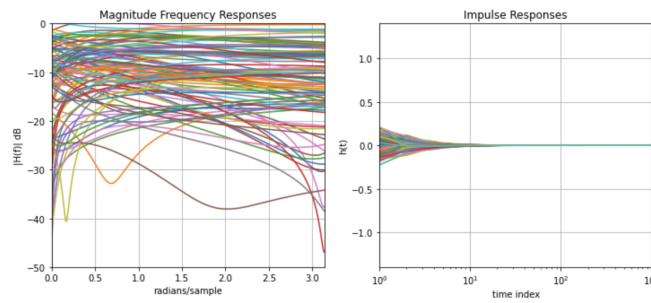


Figure 5: Frequency and impulse response for a randomly initialized FD RPE MLP with **SiLU** activations. The curves on the left side are C^∞ , and theory predicts that the curves on the right will decay at faster than any polynomial rate. They appear visually to have ‘almost’ exponential decay.

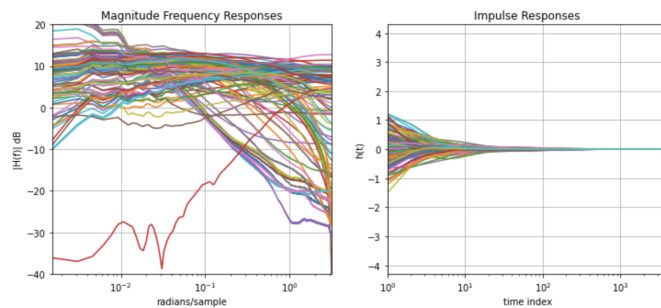
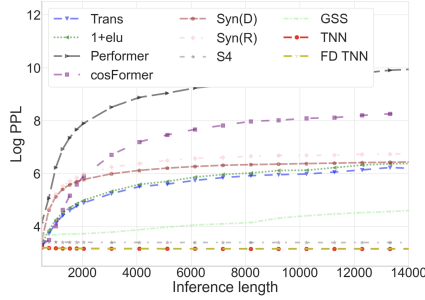
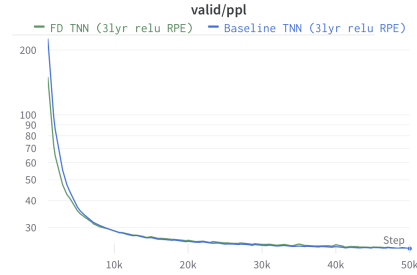


Figure 6: Frequency and impulse responses from an FD RPE MLP with **ReLU** activations, taken from one layer of a trained FD TNN. The curves on the left are continuous, and theory predicts that the curves on the right will be square summable. They clearly will vanish at infinity, although it is not immediately visually clear at what rate.

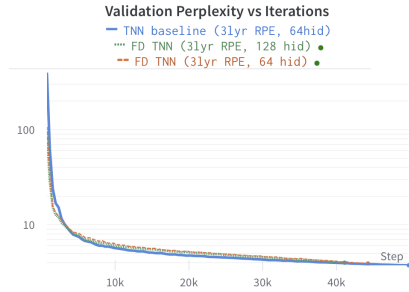


(a) Wikitext-103 Causal Pretraining.

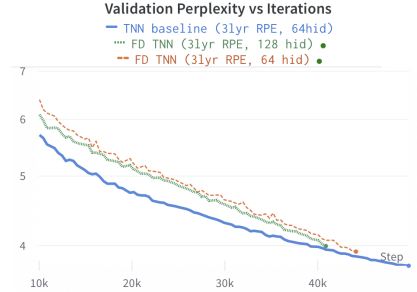


(b) Wikitext-103 Causal Pretraining.

Figure 7: a) In Wikitext-103 causal pretraining, our approach, FD TNN achieves equivalent perplexity vs inference length to TNN. b) Validation Perplexity vs iterations. In the causal setting, FD TNN converges to an equivalent quality at the same rate, but with a 5 to 15% increase in training speed depending on the RPE MLP depth (see Figure 1).



(a) Wikitext-103 Bidirectional Pretraining.



(b) Wikitext-103 Bidirectional Pretraining (close up).

Figure 8: a) In Wikitext-103 bidirectional pretraining, after minimal HP tuning from the default, we observed that FD TNN slightly lags the validation perplexity of the TNN baseline throughout much of the 50k training iterations, but closes this gap during the last 10k iterations. As our result, our 80% speed up in iterations/sec (Figure 1b) applies to wall clock time assuming one train for approximate 50k steps.

scores for the baseline in parenthesis in Table 1, next to those reported by [1]. For causal pretraining at a 512 sequence length, FD TNN achieves equivalent perplexity vs inference length as the TNN baseline (see Figure 1b). We achieve between a 5 and 15 % speed up for the causal case, and a nearly 80 % speed up in the best case (6 RPE layers) for the bidirectional case.